# A 3-D Model of Ligand Transport in a Deforming Extracellular Space

Nikola Kojić,[†] Austin Huang,[†] Euiheon Chung,[‡] Miloš Ivanović,[§] Nenad Filipović,[§] Miloš Kojić,[¶] and Daniel J. Tschumperlin[¶]*

[†]Harvard-MIT Division of Health Sciences and Technology, Cambridge, Massachusetts; [‡]Steele Laboratory, Department of Radiation Oncology, Massachusetts General Hospital, Boston, Massachusetts; [§]University of Kragujevac, Kragujevac, Serbia; and [¶]Molecular and Integrative Physiological Sciences, Harvard School of Public Health, Boston, Massachusetts

ABSTRACT   Cells communicate through shed or secreted ligands that traffic through the interstitium. Force-induced changes in interstitial geometry can initiate mechanotransduction responses through changes in local ligand concentrations. To gain insight into the temporal and spatial evolution of such mechanotransduction responses, we developed a 3-D computational model that couples geometric changes observed in the lateral intercellular space (LIS) of mechanically loaded airway epithelial cells to the diffusion-convection equations that govern ligand transport. By solving the 3-D fluid field under changing boundary geometries, and then coupling the fluid velocities to the ligand transport equations, we calculated the temporal changes in the 3-D ligand concentration field. Our results illustrate the steady-state heterogeneities in ligand distribution that arise from local variations in interstitial geometry, and demonstrate that highly localized changes in ligand concentration can be induced by mechanical loading, depending on both local deformations and ligand convection effects. The occurrence of inhomogeneities at steady state and in response to mechanical loading suggest that local variations in ligand concentration may have important effects on cell-to-cell variations in basal signaling state and localized mechanotransduction responses.

## INTRODUCTION

Cells in many tissues and organs are typically organized into relatively dense structures interconnected by specialized adhesions, but they are also separated by fluid-filled interstitial spaces that facilitate nutrient diffusion and cellular trafficking. Mechanotransduction can develop through mechanical loading-induced deformations of interstitial spaces and consequent alterations in the concentration of shed or secreted ligands in these spaces (1,2). In support of this mechanism, we previously demonstrated that the lateral intercellular space (LIS) separating cultured human bronchial epithelial cells shrinks under a constant transcellular pneumatic pressure gradient, resulting in enhanced signaling through a constitutive autocrine ligand-receptor signaling loop, consisting of epidermal-growth-factor-family ligands and the EGF receptor (1–3). A relatively simple 1-D computational model was used to illustrate how the changing dimensions of an idealized extracellular geometry alter the concentration of constitutively shed ligands in the interstitial space (1). The model enabled quantitative comparisons of biochemically measured receptor phosphorylation levels with predictions of ligand concentration changes (1,3), and it accurately predicted the magnitude and onset kinetics of measured receptor activation (3), supporting the premise of extracellular mechanotransduction occurring via increasing autocrine ligand concentration. Mechanical activation of the EGFR in airway epithelium

has been linked to increased expression of mucin proteins (4) and plays a dominant role in genomic responses to loading (3), underscoring the physiological significance of this signaling mechanism.

Although the 1-D model adequately captured the average behavior of ligands across a population of cells, it was unable to provide any insight into the local changes in ligand concentration occurring during the 3-D deformation response to mechanical loading. The development of a 3-D model is necessary to evaluate such local effects. Furthermore, a 3-D model will be essential to accurately assess cell-by-cell variations in ligand-receptor interactions as progress is made in mapping spatial and cell-specific variations in ligand shedding or secretion and receptor localization (5). Such cell-by-cell variation could be especially important in airway epithelium, which is composed of a mixture of basal, secretory, and ciliated cells, with preliminary evidence indicating that the strongest expression of EGFR occurs in basal cells (6,7). Here, we develop a 3-D numerical modeling approach and apply it to solve for the 3-D distribution of ligands in space and time in the interstitial geometry of bronchial epithelial cells during force-induced deformations. The model illustrates the heterogeneities in local ligand concentration that arise, both at steady state and during mechanical loading, due to local variations in interstitial geometry. Because EGF-family ligand-receptor interactions are pivotal in epithelial activation and differentiation, we speculate that such local variations in the ligand concentration field may play a role in specifying local cell phenotypes at baseline, and in localizing mechanotransduction responses under dynamic loading conditions.

## METHODS

### Model geometry

The key step in developing the 3-D model based on finite elements (8–11) is prescribing the nodes that define the interstitial geometry. For this purpose, we analyzed planar images of normal human bronchial epithelial cells acquired using a high-speed two-photon fast-scan microscope (see Fig. 1) (12). The interstitial space of the cultured cells was visualized with fluorescence-labeled dextran. Details of the image analysis procedure have been published previously (12). Briefly, we employed a weighted directional adaptive-thresholding method (12) to convert raw planar two-photon images into binary (black and white; see Fig. 1) images that segment the cellular and extracellular components. We found that the geometry did not differ appreciably along the apicobasal axis in serial images (12); therefore, for simplicity, we utilized a single planar image and created a pseudo-3-D geometry by extending this geometry to the approximate height of the cellular layer (see Fig. 1). In the cell culture experiments, a tonic pneumatic pressure gradient was applied at time 0, and changes in cellular and extracellular geometry were captured over subsequent minutes. As the changes in geometry were most rapid immediately after the onset of loading (3,12), and hence the greatest effects of convection and geometric heterogeneity would occur during this time period, we focused our modeling efforts on the first two time points at which images were acquired (0 and 20 s). Based on our empirical observations, we assumed that the LIS geometry deforms uniformly along the apicobasal $z$ axis (12).

In Fig. 1 $a$, the white pixels in the image represent the initial LIS geometry before mechanical loading. A segmented image of the same cells acquired 20 s after application of tonic pressure is shown in Fig. 1 $b$. A region containing the central cell and its six neighbors was selected for further analysis and within this region the LIS coordinates were obtained at both time points. Minor adjustments of the analyzed image were performed to ensure LIS continuity (experimentally observed in previous imaging studies (2,12)) and a set of boundaries was determined for each cell (see Fig. 1, $lower$). Smoothing was performed to avoid extremely complex geometries (e.g., spikes or protrusions) at the submicron level that are likely artifacts due to the limitation of the imaging system and the analysis process. The postprocessing of the images performed was in line with our previously published algorithm (12) and only slightly differed from the original, experimentally obtained image (compare Fig. 1, $upper$ and $lower$). The minor adjustments to the experimentally obtained LIS boundaries enabled the avoidance of numerical problems that arise due to the inherent mesh dependence of the finite-element method, which requires that the position of each node be accounted for and tracked throughout the time course (11).

The analyzed boundaries of the LIS (Fig. 1, $lower$) were then converted into nodal coordinates for the finite elements by subdividing each boundary into a smaller number of line elements so that each coordinate of an individual contour for $t = 0$ had a corresponding coordinate in the $t = 20$ s contour (see Fig. 2). In our model representation, we have the group of seven cells (Fig. 2, $empty$ $spaces$) surrounded by a fluid-filled LIS space that is continuous with an underlying fluid reservoir. For completeness and simplicity the outermost lateral boundary of the seven cell grouping was assumed to be closed and impermeable. The model geometry was based on our previously published experimental setup wherein normal human bronchial epithelial cells were cultured on a porous substrate connected to an underlying media reservoir (2). Apically, the cells formed tight junctions and were exposed to air, meaning that they were fed via the reservoir below, whereas the shedding of ligand into the LIS occurred along the basolateral cell walls, i.e., along the LIS boundary.

### Boundary conditions

The following boundary conditions were implemented: 1), at the bottom of the reservoir the ligand concentration was zero; 2), the top layer of the reservoir adjacent to the basal cell surfaces was assumed to be imperme-

able, excluding the continuous fluid pathways linking the interstitial spaces to the reservoir; 3), ligands were constitutively shed from the lateral cell surfaces (lateral boundaries of the LIS) at a continuous rate of $q = 10$ molecules/cell/min that was uniformly distributed along the boundary; and 4), the apical LIS surface was considered to be impermeable due to tight junctions (1). Although we assume uniform and constant shedding from all lateral cell surfaces, the model can easily incorporate spatial and time-varying shedding rates, as such data become available.

### Governing equations

To model ligand concentration dynamics (as well as the steady-state case with zero velocities (Fig. 3)), we computed the 3-D diffusion equations using an approach analogous to that followed for the previously published 1-D model (1). However, we now employed 3-D finite elements (see white lines in Fig. 3) to solve the governing 3-D transport equations (13,14):

LIS:

$$\frac{\partial C}{\partial t} = D_{LIS}\left(\frac{\partial^2 C}{\partial x^2} + \frac{\partial^2 C}{\partial y^2} + \frac{\partial^2 C}{\partial z^2}\right) - \left(V_x\frac{\partial C}{\partial x} + V_y\frac{\partial C}{\partial y} + V_z\frac{\partial C}{\partial z}\right).$$
(1a)

Reservoir:

$$\frac{\partial C}{\partial t} = D_{out}\left(\frac{\partial^2 C}{\partial x^2} + \frac{\partial^2 C}{\partial y^2} + \frac{\partial^2 C}{\partial z^2}\right) - \left(V_x\frac{\partial C}{\partial x} + V_y\frac{\partial C}{\partial y} + V_z\frac{\partial C}{\partial z}\right).$$
(1b)

Here, the ligand concentration, $C$, is a function of both time and the three spatial coordinates $x$, $y$, and $z$. We utilized linear 3-D elements because they are the most robust, widely used, and accurate for fine meshes (15). The 3-D elements were previously validated on benchmark cases by matching analytical solutions (11), and mesh independence was established by observing that the results differed by several percent in the LIS when the number of elements was doubled (see Fig. S1 in the Supporting Material).

As in the previous 1-D model, the diffusivity of the ligand in the LIS (hindered diffusion, $D_{LIS}$) differs from the diffusivity in the reservoir (free diffusion, $D_{out}$) (1), but in the 3-D model, the net ligand shedding term is not present in the governing LIS equation, because ligand shedding into the LIS is prescribed as a surface flux on the cell boundary. To solve Eq. 1, we first considered the 3-D velocity field (i.e., velocities $V_x$, $V_y$, and $V_z$ in Eq. 1) based on the Navier-Stokes equations (16) for a viscous, incompressible fluid:

$$\rho\left(\frac{\partial V_i}{\partial t} + \frac{\partial V_i}{\partial x_k}V_k\right) = -\frac{\partial p}{\partial x_i} + \mu\frac{\partial^2 V_i}{\partial x_k \partial x_k}$$
$$i = 1, 2, 3; \text{sum on } k : k = 1, 2, 3,$$
(2)

where $\rho$ is fluid density, $p$ is fluid pressure, $\mu$ is fluid viscosity, and the indices $i$ and $k$ each correspond to the directions $x$, $y$, and $z$.

To eliminate fluid pressure $p$ in Eq. 2, we employ the standard penalty method and introduce a large parameter, $\lambda$, and approximate the continuity equation as (8)

$$\frac{\partial V_i}{\partial x_i} + \frac{p}{\lambda} = 0 \text{ sum on i : i} = 1, 2, 3$$
(3)

This form of approximation was introduced by Zienkiewicz and Reddy (17,18) and was the subject of many subsequent investigations (e.g., Dhatt and Hubert (19)). The penalty parameter, $\lambda$, can physically be considered as
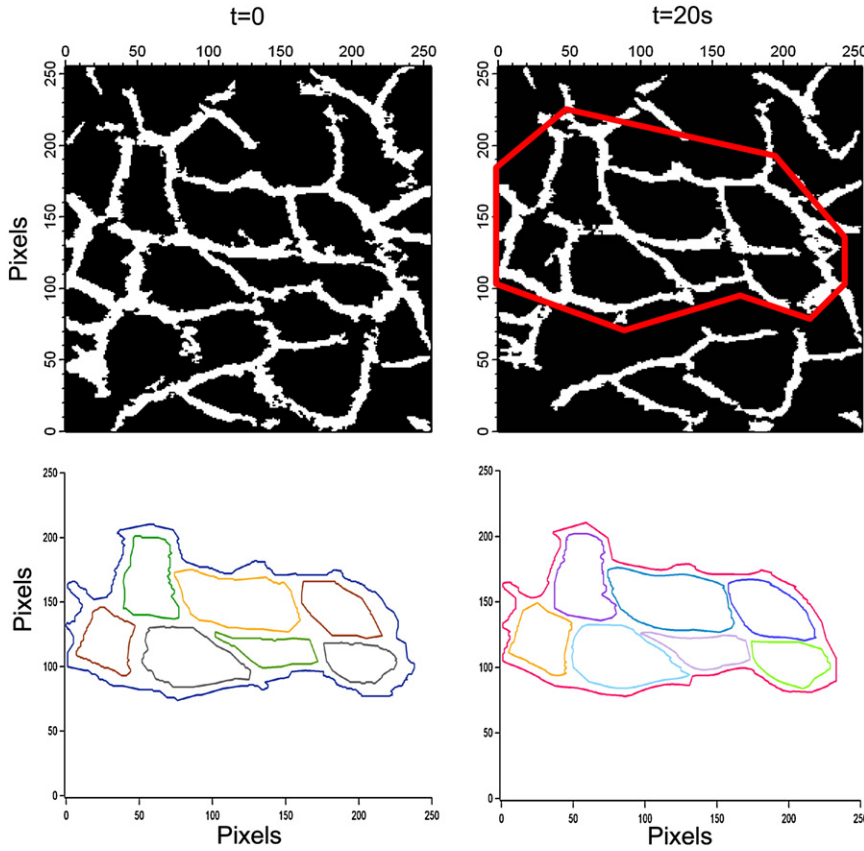
FIGURE 1 (*Upper*) Analyzed image at t = 0 (before pressure application) and the corresponding image after application of continuous, constant pressure of 30 cmH$_2$O for t = 20 s. White pixels indicate the LIS and black pixels the cellular space. A region of seven cells (*red outline*) was chosen. (*Lower*) The coordinates of the LIS boundary within this region were determined for both t = 0 and t = 20 s images, after manual smoothing and corrections to ensure a continuous LIS. Axis markers indicate the number of pixels, where 1 pixel =~0.3 $\mu$m.

the fluid bulk modulus allowing small compressibility, whereas mathematically it corresponds to the penalty constraint approach in solving differential equations. Upon substitution for pressure $p$ in Eq. 2, we obtain the modified Navier-Stokes equations

$$\rho\left(\frac{\partial V_i}{\partial t} + \frac{\partial V_i}{\partial x_k}V_k\right) = \lambda\frac{\partial^2 V_k}{\partial x_i \partial x_k} + \mu\frac{\partial^2 V_i}{\partial x_k \partial x_k} \qquad (4)$$
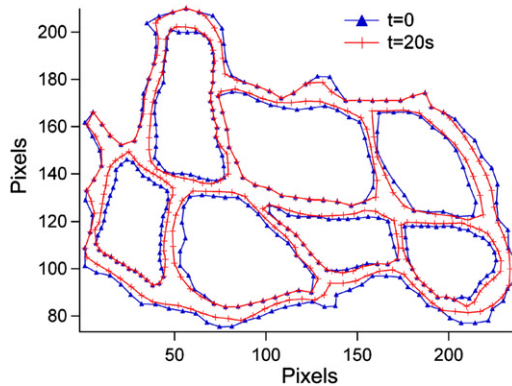
$$i = 1,2,3; \text{sum on } k: \; k = 1,2,3$$



FIGURE 2 LIS boundaries from Fig. 1 (*blue*, t = 0; *red*, t = 20 s) subdivided into equal numbers of line segments. Symbols (*triangles* and *perpendicular lines*) represent nodes for finite elements in the 3-D model. Each symbol in the t = 0 line has a corresponding marker in the t = 20 s line. Symbols indicate the number of pixels, and 1 pixel = 0.3 $\mu$m.

After applying the standard Galerkin procedure (11) to Eq. 4, the corresponding finite-element equation is

$$\mathbf{M}\dot{\mathbf{V}} + (\mathbf{K}_{vv} + \mathbf{K}_{vv}^{\lambda})\mathbf{V} = \mathbf{F}_v + \mathbf{F}_{\lambda}, \qquad (5)$$

where

$$M_{KJ} = \int_V \rho N_K N_J dV, \qquad (6)$$

with $K, J = 1,..,$ and $N$ is the number of nodes

$$\left[(\mathbf{K}_{vv})_{KJ}\right]_{ii} = \left[\rho\int_V N_K N_{J,j}\,V_j dV\right]_{ii} + \left[\int_V \mu N_{K,j}N_{J,j}dV\right]_{ii},$$
$$\text{no sum on } i \qquad (7)$$

$$(\mathbf{K}_{vv}^{\lambda})_{KiJj} = \lambda\int_V N_{K,i}N_{J,j}dV, \qquad (8)$$

$$(\mathbf{F}_{\lambda})_{Ii} = \lambda\int_S N_I V_{j,j}n_i dS \qquad (9)$$

$$(\mathbf{F}_v)_{Ki} = \int_V N_K f_i^V dV + \int_S N_K(-p\delta_{ij} + \mu V_{i,j})n_j dS \quad (10)$$
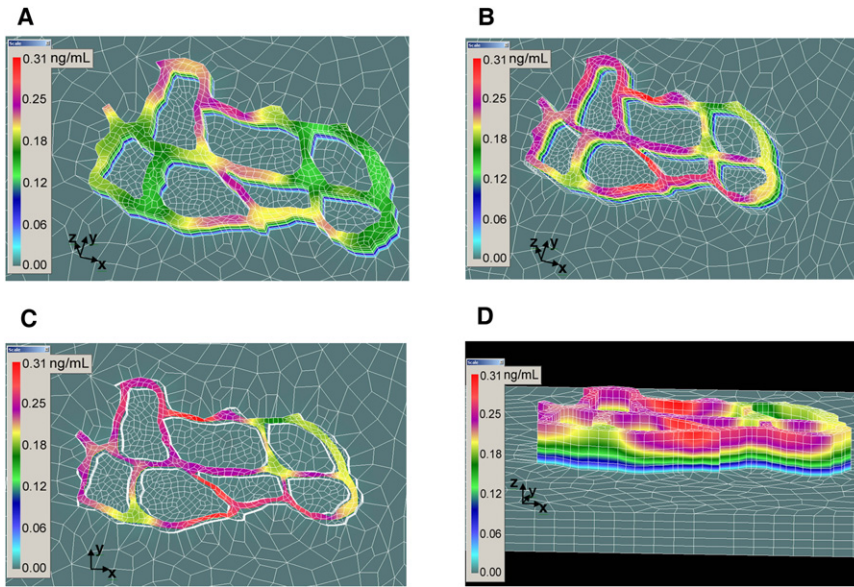
**A**



**B**

**C**

**D**

FIGURE 3 (*A*) Oblique view of the steady-state HB-EGF concentration (scale bar at left (ng/mL)) for the initial, precollapse geometry (see Fig. 2 contours). Lines indicate finite-element boundaries. LIS height and reservoir depth were both 15 $\mu$m. Parameters and boundary conditions: $D_{LIS}$ = 1.8 $\mu$m$^2$/s and $D_{reservoir} = D_{out}$ = 75 $\mu$m$^2$/s; ligands constitutively shed into LIS from cell surface at a rate of $q$ = 10 molecules/cell/min; ligand concentration was zero at the bottom of the reservoir; the most apical LIS surface and top layer of reservoir were impermeable walls. (*B*) An oblique view of the concentration field at t = 20 s for the collapse in geometry of Fig. 2. (*C*) A top-down view along the apicobasal axis, where white boundaries indicate the t = 0 geometry (Fig. 2, *triangles*), whereas colored boundaries correspond to the t = 20 s geometry (Fig. 2, *perpendicular lines*). (*D*) A nearly edge-on view, showing the LIS height and the bottom reservoir. Scale bars in *A–D* indicate concentration in ng/mL.

Here, $f_i^V$ is the volumetric force (force/unit volume) and $\delta_{ij}$ is the Kronecker symbol (11).

In Eqs. 6–9, $N_K$ and $N_J$ are the interpolation functions, and the notation $N_{J,j}$ indicates the spatial derivative of the interpolation functions in the *j*-direction, whereas the double index *Ki* means node *K* and component *i*, and so on. The terms *ni* and *nj* in Eqs. 9 and 10 represent the unit normal in the *i* and *j* directions, respectively, on the element surface, *S*.

In parallel with solving the above equations for fluid flow, we solve governing finite-element equations obtained from Eq. 1:

$$\widehat{\mathbf{M}}\dot{\mathbf{C}} + \widehat{\mathbf{K}}\mathbf{C} + \mathbf{K}_{Cv}\mathbf{V} = \mathbf{Q}^S, \tag{11}$$

where

$$\widehat{M}_{KJ} = \int_V N_K N_J dV \ , \ \widehat{K}_{KJ} = \int_L DN_{K,i}N_{J,i}dV \ , \text{ and}$$
$$Q_K^S = \int_S N_K q_S dS \tag{12}$$

and

$$\mathbf{K}_{Cv} = \left[ (\mathbf{K}_{Cv})_1 (\mathbf{K}_{Cv})_2 (\mathbf{K}_{Cv})_3 \right] \ ,$$
$$(\mathbf{K}_{Cv})_{KJ \ i} = \int_V \frac{\partial C}{\partial x_i} N_K N_J dV \tag{13}$$

The above equations were then solved incrementally and iteratively using the software package PAK-F (20) for both the steady-state (zero velocity) case of Fig. 3 and during mechanical loading-induced change in LIS geometry. To investigate how ligand concentrations (and the velocity field) vary during loading, we incorporated the geometry 20 s after the application of a transcellular pressure gradient of 30 cm H$_2$O (see Fig. 2, *red lines* and *symbols*). We assumed that between t = 0 and t = 20 s the position of each node (i.e., Fig. 2, *symbols*) changed linearly with time, meaning that if the *x,y* coordinates of a node were (0,0) at t = 0 and (20,20) at t = 20 s, then at t = 10 s, the node was halfway in between, at ((*x*20 − *x*0)/2,(*y*20 − *y*0)/2). This approach

yielded LIS geometries for each time step, and hence we could track each finite-element node position through time.

## RESULTS

### Steady-state 3-D ligand concentration

The 3-D model was constructed by extending the 2-D representation of Fig. 2 to a height (*z*-dimension) of 15 $\mu$m, with an underlying reservoir that extended 15 $\mu$m below the LIS (see Fig. 3). The coordinates (i.e., symbols) from Fig. 2 served as nodes for finite elements on the LIS boundaries, while the inside of the LIS was discretized using a PAK mesh-generation algorithm (see Fig. 3, where the white lines represent the 3-D finite elements with the nodes at the intersections).

We solved for the steady-state concentration when $D_{LIS}$ = 1.8 $\mu$m$^2$/s and $D_{reservoir} = D_{out}$ = 75 $\mu$m$^2$/s, which assumes hindered diffusion of HB-EGF ligand in the LIS and unhindered, free diffusion in the reservoir (1), with the resulting ligand concentration profile for the initial geometry (see Fig. 2, *blue lines* and *symbols*) shown in Fig. 3. This steady-state solution assumed a fixed geometry (no fluid flow) and thus, all of the velocities in the diffusion and fluid-flow equations (Eqs. 2–4) were zero. A more detailed, 3-D depiction of the model results can be found in Movie S1 and Movie S2.

### The 3-D fluid velocity field

To solve for the velocity field of the fluid (Eqs. 4–9) induced by mechanical loading, we assumed that: 1), the velocity of the fluid at the wall boundary was equal to that at the LIS wall; 2), the apical LIS surface and the top layer of the reservoir adjacent to the basal cell surfaces were impermeable

walls; and 3), all of the fluid that exits the LIS appears in the reservoir. The solved velocity field at 20 s of loading (corresponding to a change in geometry from the blue (t = 0) to the red (t = 20 s) contours in Fig. 2) is shown in vector form in Fig. 4. The top-down (apicobasal) view in Fig. 4 reveals velocities in the $xy$ plane caused by the change in LIS geometry. The oblique view of the velocity field indicates that the largest velocities are in the apicobasal $z$-direction, as expected. However, the presence of considerable velocities in the $xy$ plane results in an overall complex 3-D fluid field that directly affects the ligand concentration (see Eq. 1). For a multiview 3-D representation of the velocity field, see Movie S1 and Movie S2.

## 3-D ligand concentration during mechanical loading

We solved for the time-varying 3-D ligand concentration field (Eqs. 1 and 10–12) as a function of the mechanical loading induced change in LIS geometry, with the results at t = 20 s displayed in Fig. 3. To compare the local ligand concentration with the undeformed and deformed LIS geometry, see the top-down view (Fig. 3, *lower*), where the initial (t = 0) geometry is indicated by the white lines surrounding the edges of the colored (t = 20 s) geometry.

It should be noted that in a given LIS element, there is typically approximately one molecule of heparin-binding EGF (HB-EGF) ligand, since the concentration is given in units of ng/mL and the volume of a finite element is ~50 $\mu m^3$. Thus, for HB-EGF with a molecular mass of 22 kDa, there is ~$2 \times 10^{-24}$ mole in a finite element, which when multiplied by Avogadro's number yields ~1.2 molecules of HB-EGF/element.

## 3-D ligand concentration during a more rapid change in geometry

Since our previous results (1) indicate that the rate of LIS collapse is the dominant parameter influencing ligand transport dynamics, we performed a similar analysis with the same change in geometry occurring linearly over a 1-s collapse (Fig. 5). Although the overall appearance is not dissimilar to that shown in Fig. 3, apparent in the figure are focal zones of increased concentration (Fig. 5, *asterisks*), which we term hotspots, caused by the velocity field evoked by the rapid geometric change (Fig. 6). This velocity field is more complex than that for the 20-s collapse (see Fig. 4), with velocities greater by an order of magnitude and larger contributions of the $x$ and $y$ components.

To examine in more detail the concentration within the LIS, we graphically displayed the concentration field for a prescribed segment of Fig. 5 after virtual cutting with planes parallel to the apicobasal axis (see Fig. 7). The cutting planes went along the boundaries of finite elements (hence the jagged-edge appearance) (Fig. 7, *upper*). Note
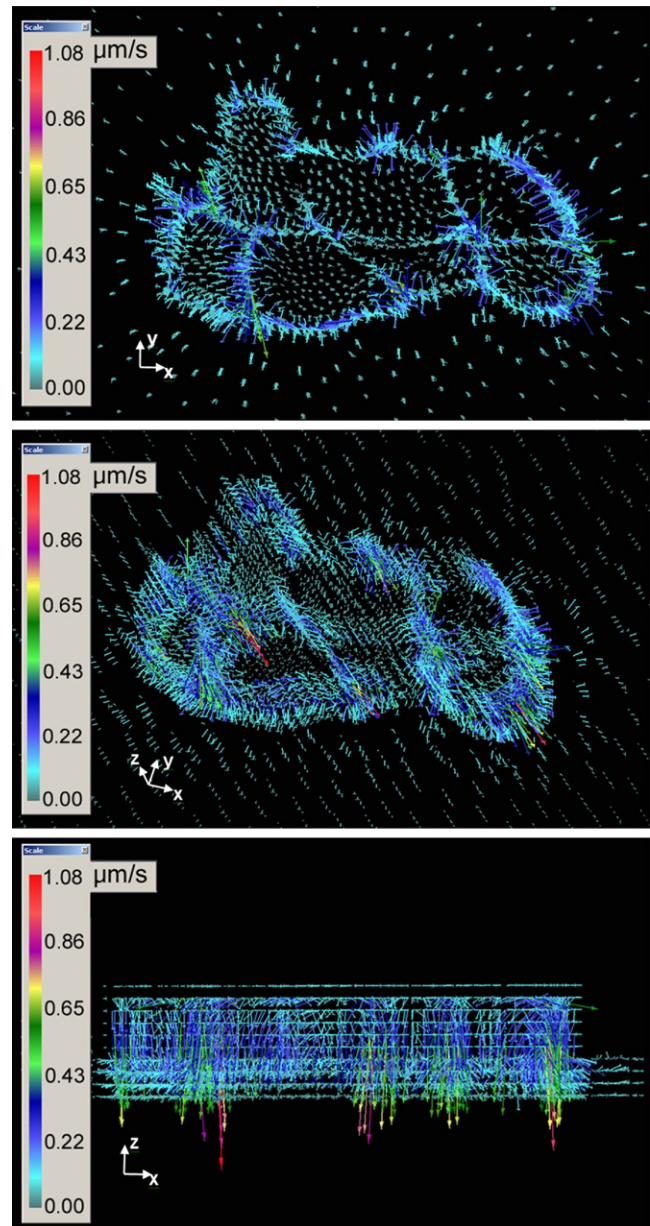


FIGURE 4 Velocity field at t = 20 s for the collapse in geometry of Fig. 2 displayed in vector form, where shade and length indicate intensity. (*Upper*) Top-down view along the apico-basal axis of the velocity vectors. (*Middle*) Oblique view. (*Lower*) Edge-on view showing that the largest velocities are in the apicobasal direction. Scale bars indicate velocity in $\mu m/s$.

the local heterogeneities in concentration profile when the segment is viewed in the apicobasal plane (Fig. 7, *lower*), especially near the basal cell surfaces. Corresponding locations in the two views (Fig. 7, *upper* and *lower*) are represented by asterisks, and the nonuniform zones (e.g., above the red asterisk (Fig. 7, *lower*)) indicate concentration hotspots where, largely due to convective effects, a prominent local increase in concentration occurs.

In all of the above results, we focused on absolute concentration values, but the relevant biological stimulus is the
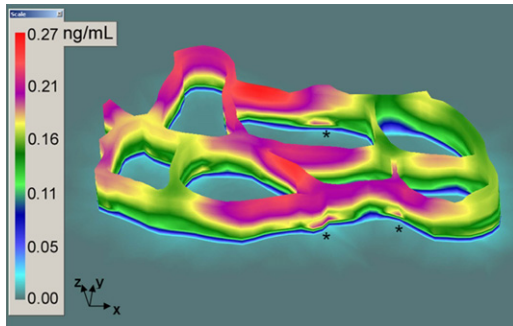
FIGURE 5 Oblique view of the calculated concentration field at the end of a 1-s collapse for the geometry of Fig. 2. Asterisks indicate three hotspots (zones with increased concentration) visible from this view. For clarity, the finite-element mesh was omitted. Scale bar, concentration in ng/mL.

change in concentration relative to local baseline. Thus, for both the 1- and 20-s cases, we plotted the difference between the final concentration field and the initial steady-state concentration (see Fig. 8). The scale bars are identical in Fig. 8, so the magnitudes of the relative concentrations (i.e., the colors in the scale bars) can be compared between the 1-s and 20-s images (Fig. 8, *upper* and *lower*, respectively). The 1-s image (Fig. 8, *upper*) was obtained by subtracting the steady-state concentration (Fig. 3 *A*) from the concentrations at the end of 1 s (Fig. 5), whereas the 20-s image represents the difference between the steady-state and 20-s concentrations (Fig. 3, *A* and *B*, respectively).

The 3-D model presented in this article builds on a previously published 1-D model (1). Briefly, the 1-D model represents the LIS by using two parallel plates separated by a characteristic LIS width, whose collapse over time matches the collapse in LIS volume over time. To compare the 1-D and 3-D models, we input the same dynamics of LIS volume collapse (i.e., 33% difference in LIS areas for t = 0 and t = 20 s of Fig. 1) into the 1-D model, and employed the same diffusion coefficients as in the 3-D model. Fig. 9 (*upper*) shows the 1-D steady-state and 20-s ligand concentration profiles (*red* and *blue solid lines*, respectively) obtained from the model. The fold change in ligand concentration relative to the initial, steady-state value (which we term normalized LIS concentration) was calculated at each node in the 1-D (*dashed blue line*) and 3-D models. The distributions of nodal changes in ligand concentration for the 1-D and 3-D model were then plotted together for comparison (Fig. 9). The mean and median values of the normalized LIS concentrations were 1.36 and 1.29, respectively, for the 1-D model and 1.28 and 1.26, respectively, for the 3-D model. Although the mean and median fold changes in ligand concentration were closely matched in the two models, the distribution was greatly expanded in the 3-D model, reflecting both the local heterogeneities in LIS dimensions and deformations and the nontrivial influence of convection on the ligand concentration field (see Fig. 4 and Fig. S2).
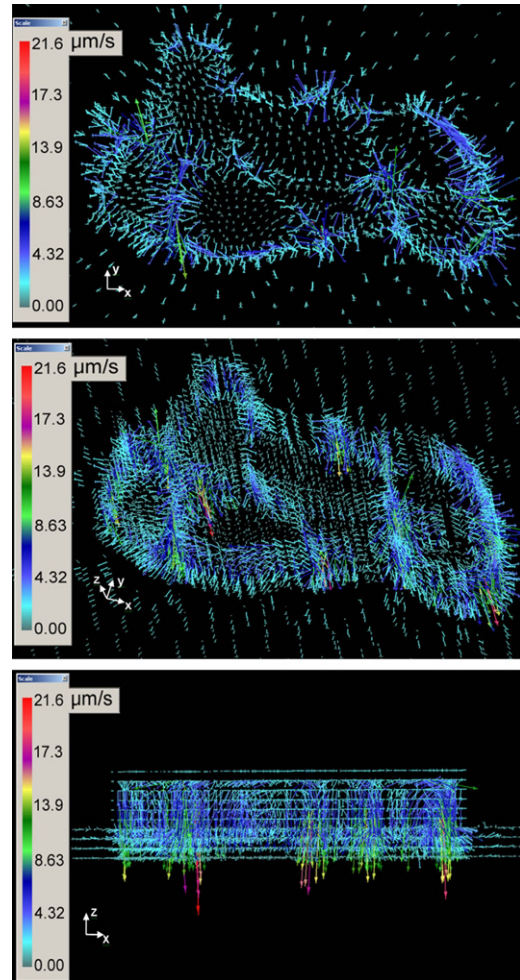


FIGURE 6 Velocity field for the 1-s collapse in LIS geometry. (*Upper*) Top-down view along the apicobasal axis of the velocity vectors. (*Middle*) Oblique view. (*Lower*) Edge-on view showing that the largest velocities are in the apicobasal direction. Scale bars, velocity in μm/s.

## DISCUSSION

We have developed a 3-D computational modeling approach that allows us to calculate the 3-D spatial variations in ligand concentration within a realistic geometry extracted from two-photon imaging of an epithelial interstitium (12). In principle, this technique could be exploited to calculate ligand distributions in the presence of spatiotemporal gradients in ligand shedding rates, ligand consumption, ligand diffusion, and interstitial geometry. In these simulations, we assumed uniform shedding of ligands from all lateral cell surfaces and were able to observe the steady-state spatial gradients in ligand concentration that emerge as a consequence of heterogeneities in the interstitial geometry. Because mechanical loading can dynamically alter the interstitial geometry, as we showed previously (2), we used the model to calculate the change in ligand concentration field that occurs in response to identical changes in interstitial geometry occurring over two time intervals. To do so,
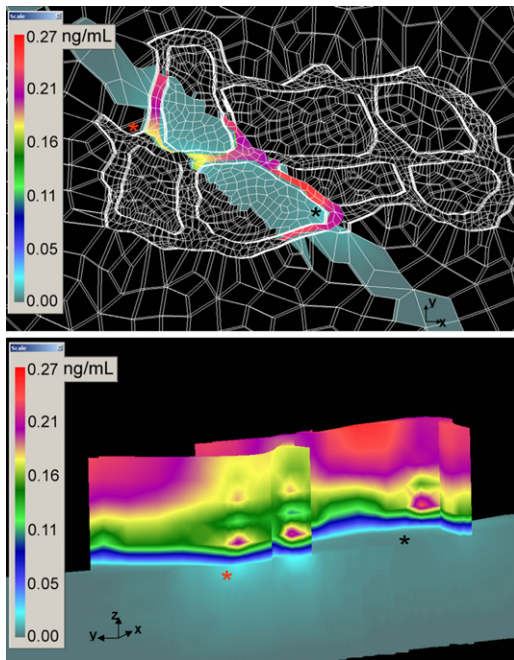
FIGURE 7 A segment of Fig. 6. (*Upper*) Top-down view of the selected segment, with finite-element mesh (*lines*) included to indicate the segment chosen. (*Lower*) Enlarged, edge-on view of the segment. Asterisks represent the corresponding locations in the two views. Nonuniform zones (e.g., above asterisks) indicate concentration hotspots.



FIGURE 8 Relative concentration fields obtained by subtracting the initial precollapse concentration (same for both cases (see Fig. 3 *A*)) from the concentration at the end of a collapse: C(t = end of collapse) − C(t = 0). (*Upper*) Relative concentrations at the end of a 1-s collapse (nonuniform areas indicate concentration hotspots). (*Lower*) Relative concentrations at the end of a 20-s collapse. Scale bars (concentration in ng/mL) are identical, so scales can be used for comparison between the relative concentrations for 1-s and 20-s collapse.

we solved for the interstitial fluid flow (via the 3-D Navier-Stokes equations) and directly coupled it to the ligand transport equations. Our major findings are that 1), the steady-state ligand concentration is heterogeneously distributed as a function of the nonuniform interstitial geometry; 2), for relatively slow changes in interstitial geometry, where convection plays a minor role, the changes in ligand concentration are homogeneously distributed; and 3), in more rapid scenarios, the local changes in ligand concentration are highly nonuniform, resulting in the formation of concentration hotspots. Based on these findings, we conclude that our previous 1-D model adequately captures the overall change in ligand concentration when changes in interstitial geometry occur over tens of seconds or more (1,3), though with subtle differences in the overall distribution of ligand concentration changes distributed across model geometries. However, the 3-D model provides essential insight into ligand transport occurring during rapid changes in interstitial geometries, as exemplified by the short-duration case of 1 s.

The 3-D model has several limitations at present: the assumptions of uniform LIS geometry along the apicobasal axis and uniform net ligand shedding throughout the LIS, as well as the use of a continuum model that yields concentration values of only a few ligand molecules in the LIS between two cells. These limitations could be overcome in future models with the aid of finer-resolution imaging techniques to fully capture the true 3-D nature of the LIS geometry, along with application of novel imaging modalities to
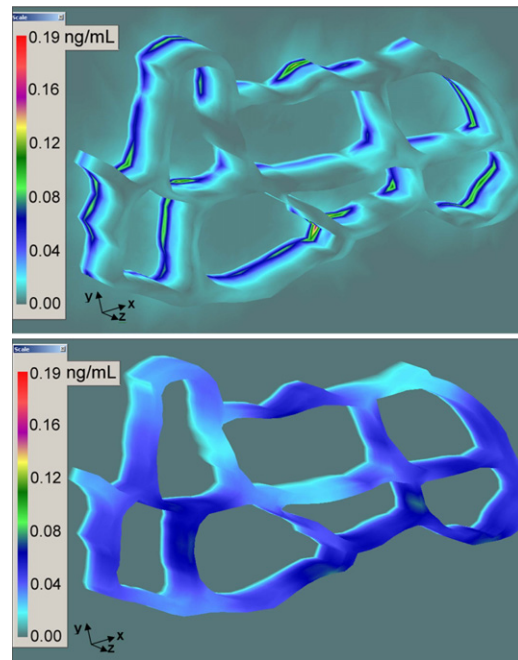
quantify the rate of ligand shedding and consumption on an individual cell level (5). With these measurements in place, stochastic models of ligand-receptor binding and unbinding on a submicron scale (21,22) could be coupled to our current 3-D model to yield more information on the intricate time- and space-varying mechanotransduction events that occur locally in neighboring cells.

Comparison of the 3-D model simulations under the two different deformation scenarios (1 s vs. 20 s) provides a key new insight into mechanotransduction by epithelial cells. Our results demonstrate that under certain conditions, either localized or global mechanoresponses can emerge in the presence of a uniform mechanical stimulus. Our model can aid future efforts aimed at examining how these individual cell-by-cell responses are orchestrated into a unified response on the tissue level. We focused on the 20-s case, because it directly corresponds to the time course of LIS geometry changes observed under in vitro loading. The same deformation occurring over 1 s has not been observed in vitro, but it is entirely plausible based on bronchospasm or vasospasm observed in situ. The change in ligand concentration field is profoundly influenced by the rate of change of LIS dimensions, which dictates the character and magnitude of the ensuing fluid flow (see Figs. 4 and 6). For the rapid, 1-s collapse, this results in the formation of concentration
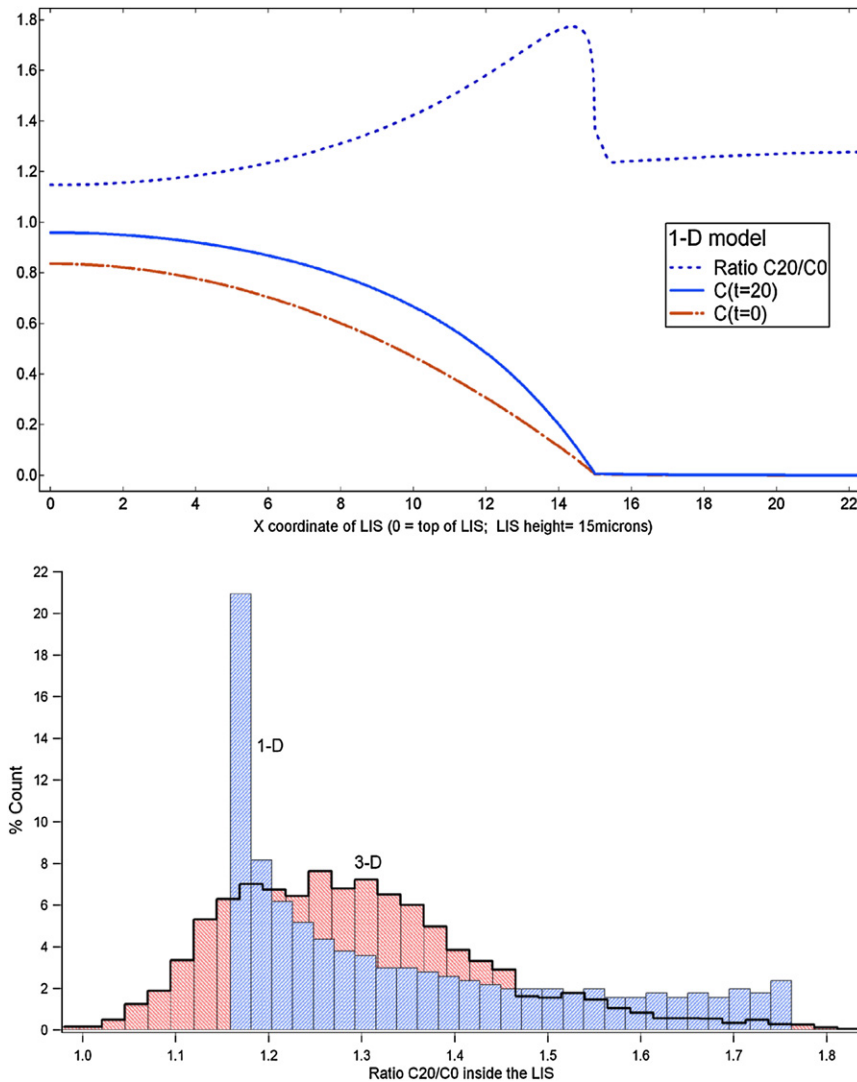
FIGURE 9 (*Upper*) 1-D model results for a t = 20 s collapse showing the precollapse concentration profile at t = 0 (*red line*), the end-of-collapse concentration profile at t = 20 s (*blue solid line*), and the normalized concentration, i.e., the ratio of the end-of-collapse profile to the initial profile (*blue dashed line*). The mean and median for the 1-D model normalized LIS concentration values were 1.36 and 1.29, respectively (1.28 and 1.26, respectively, for the 3-D model). Units for y-axis values <1 are in ng/mL; values >1 are the ratio. (*Lower*) Histograms of the normalized LIS concentrations (relative to initial) at the end of the collapse (t = 20 s) for the 1-D and 3-D models.

hotspots (see Figs. 5 and 7), especially near the basal cell surface, which yield a concentration profile dramatically different from the well-preserved parabolic profile of the 20-s case (see Figs. 3 and 8). The formation of these hotspots was surprising and could facilitate a better understanding of how cells and tissues respond to a rapid change in geometry. For example, such hotspots could indicate that mechanical loads applied over a population of cells may be transduced most effectively within a subpopulation of cells, or even at particular surface locations on single cells, potentially leading to polarized cellular responses to an otherwise homogenously applied load. Alternatively, signaling in hotspots may need to be amplified and transmitted to surrounding cells through paracrine signaling to provide the appropriate population-level tissue responses.

Based on these findings, we conclude that the 3-D model advances our knowledge by providing unique insight into local variations of ligand concentration that occur during dynamic changes in interstitial geometries. Furthermore,

the different distributions of ligand changes (see Fig. 9, *lower*) emerging from the 1-D and 3-D cases indicate that modeling only the average LIS collapse for a population of cells (as in the 1-D model) obscures the underlying normal distribution present within a realistic 3-D geometry. Such a normal distribution is to be expected for biological systems and thus must be accounted for in numerical models that hope to capture cell-specific mechanotransduction processes.

The results from the 3-D simulations emphasize that variations in interstitial geometry introduce heterogeneous ligand concentration fields under both steady-state conditions and in response to mechanical loading. These inhomogeneities may be particularly important in the context of the airway epithelium, where a mixed population of ciliated, mucous secretory, and basal cells coexist in close proximity (23). Because EGFR signaling is clearly linked to expression of various epithelial phenotypes (24,25) and plays a role in the increased expression of mucus proteins in response to chronic mechanical loading (4), we speculate

that local variations in ligand concentration may play a role in forming and perturbing the pattern of cell populations present in the airways. In a similar context, local variations in morphogen production, diffusion, and consumption are increasingly seen to be important factors in development, tissue differentiation, and cell fate decisions (5). As the local distribution of ligands, receptors, and ligand diffusion characteristics in these scenarios become increasingly accessible, the 3-D modeling approach detailed here will provide an ideal tool to generate insight into the distribution of signaling events ongoing under various physiological or pathophysiological perturbations.

## SUPPORTING MATERIAL

Two figures and two movies are available at http://www.biophysj.org/biophysj/supplemental/S0006-3495(10)01194-X.

## REFERENCES

1. Kojić, N., M. Kojić, and D. J. Tschumperlin. 2006. Computational modeling of extracellular mechanotransduction. *Biophys. J.* 90:4261–4270.

2. Tschumperlin, D. J., G. Dai, …, J. M. Drazen. 2004. Mechanotransduction through growth-factor shedding into the extracellular space. *Nature.* 429:83–86.

3. Kojic, N., E. Chung, …, D. J. Tschumperlin. 2010. An EGFR autocrine loop encodes a slow-reacting but dominant mode of mechanotransduction in a polarized epithelium. *FASEB J.* 24:1604–1615.

4. Park, J. A., and D. J. Tschumperlin. 2009. Chronic intermittent mechanical stress increases MUC5AC protein expression. *Am. J. Respir. Cell Mol. Biol.* 41:459–466.

5. Yu, S. R., M. Burkhardt, …, M. Brand. 2009. Fgf8 morphogen gradient forms by a source-sink mechanism with freely diffusing molecules. *Nature.* 461:533–536.

6. Ross, A. J., L. A. Dailey, …, R. B. Devlin. 2007. Transcriptional profiling of mucociliary differentiation in human airway epithelial cells. *Am. J. Respir. Cell Mol. Biol.* 37:169–185.

7. Staudt, M. R., J. A. Fuller, …, R. G. Crystal. 2010. Whole transcriptome analysis of human airway epithelial basal cells. *Am. J. Respir. Crit. Care Med.* 181:A6402.

8. Huebner, K. H. 1975. The Finite Element Method for Engineers. John Wiley and Sons, New York.

9. Hughes, T. J. R. 1987. The Finite Element Method. Linear Static and Dynamic Finite Element Analysis. Prentice Hall, Englewood Cliffs, NJ.

10. Kojic, M., and K.-J. Bathe. 2005. Inelastic Analysis of Solids and Structures. Springer-Verlag, Berlin.

11. Kojic, M., N. Filipovic, …, N. Kojic. 2008. Computer Modeling in Bioengineering: Theoretical Background, Examples and Software. John Wiley & Sons, Chichester, United Kingdom.

12. Kojic, N., A. Huang, …, P. T. So. 2008. Quantification of three-dimensional dynamics of intercellular geometry under mechanical loading using a weighted directional adaptive-threshold method. *Opt. Express.* 16:12403–12414.

13. Bird, R. B., W. E. Stewart, and E. N. Lightfoot. 2007. Transport Phenomena. John Wiley & Sons, New York.

14. Deen, W. M. 1998. Analysis of Transport Phenomena. Oxford University Press, New York.

15. Bathe, K.-J. 1996. Finite Element Procedures. Prentice Hall, Englewood Cliffs, NJ.

16. Batchelor, G. K. 1967. An Introduction to Fluid Dynamics. University of Cambridge Press, Cambridge, United Kingdom.

17. Reddy, J. N. 1982. On penalty function methods in the finite element analysis of flow problems. *Int. J. Numer. Methods Fluids.* 2:151–171.

18. Zienkiewicz, O. C. 1974. Constrained variational principles and penalty function methods in finite element analysis. *In* Lecture Notes in Mathematics: Conference on the Numerical Solution of Differential Equations. G. A. Watson, editor. Springer- Verlag, Berlin.

19. Dhatt, G., and G. Hubert. 1986. A study of penalty elements for incompressible laminar flows. *Int. J. Numer. Methods Fluids.* 6:1–19.

20. Kojic, M., N. Filipovic, …, N. Grujovic. 1998. PAK-F Finite Element Program for Laminar Flow with Mass and Heat Transfer. University of Kragujevac, Kragujevac, Serbia.

21. Shvartsman, S. Y., C. B. Muratov, and D. A. Lauffenburger. 2002. Modeling and computational analysis of EGF receptor-mediated cell communication in *Drosophila* oogenesis. *Development.* 129:2577–2589.

22. Wiley, H. S., S. Y. Shvartsman, and D. A. Lauffenburger. 2003. Computational modeling of the EGF-receptor system: a paradigm for systems biology. *Trends Cell Biol.* 13:43–50.

23. Kikuchi, T., J. D. Shively, …, D. J. Tschumperlin. 2004. Differentiation-dependent responsiveness of bronchial epithelial cells to IL-4/13 stimulation. *Am. J. Physiol. Lung Cell. Mol. Physiol.* 287:L119–L126.

24. Kim, S., J. J. Shim, …, J. A. Nadel. 2002. IL-13-induced Clara cell secretory protein expression in airway epithelium: role of EGFR signaling pathway. *Am. J. Physiol. Lung Cell. Mol. Physiol.* 283:L67–L75.

25. Takeyama, K., J. V. Fahy, and J. A. Nadel. 2001. Relationship of epidermal growth factor receptors to goblet cell production in human bronchi. *Am. J. Respir. Crit. Care Med.* 163:511–516.